Article ID：1007−7294(2026)06−0853−18

Analysis Model for Pressure Wave during Spherical Projectile Water Entry considering Reflection from Preset Air Layer

WU Meng−meng[a,b], *HOU Hai−liang*[a], *LI Dian*[a], *YANG Shao−hong*[b], *LI Yong−qing*[a]
(a. College of Naval Architecture and Ocean Engineering; b. Department of Basic Course, Naval University of Engineering, Wuhan 430033, China)

Abstract: To analyze the propagation of pressure waves generated during spherical projectile water entry within liquid-filled structures, this study establishes a computational model for the pressure wave considering reflection from a preset air layer. The model combines the virtual and real mirror methods with potential flow theory, and its accuracy is validated through numerical simulations. Using the established model, the propagation processes of the pressure wave during projectile water entry within liquid-filled structures configured with either a top air layer or a centrally located spherical air layer are examined. The effects of air layer height h, spherical air layer center location D and radius r on the strength and propagation of the pressure wave in water are analyzed. The results show that the rarefaction wave reflected from the air layer interface induces a truncation effect on the pressure wave propagation, significantly reducing the duration of positive pressure and the specific impulse. Moreover, the specific impulse decreases as h and r increase. A smaller D leads to more significant attenuation of the initial pressure wave specific impulse, while a larger D results in more noticeable attenuation of the secondary pressure wave peak and its specific impulse.

Key words: spherical projectile; water entry; pressure wave; preset air layer; truncation effect
CLC number：O342 **Document code**：A **doi:** 10.3969/j.issn.1007−7294.2026.06.002

0 Introduction

During the penetration of a projectile into a liquid-filled structure, part of the projectile's kinetic energy is converted into the pressure potential energy and kinetic energy of the liquid, generating intense pressure waves and liquid flow, a phenomenon known as hydrodynamic ram (HRAM). The combined effect of HRAM with the projectile can cause large-scale rupture or explosion of the structure, resulting in catastrophic consequences. Examples include the impact and penetration of high-speed fragments entering aircraft fuel tanks[1], the impact and penetration of space debris impacting spacecraft pressure vessels[2], and the impact on flammable or toxic liquid-filled tanks by terrorists[3]. To mitigate structural damage under high-velocity impact, air layers can be preset within liquid-filled structures. Taking advantage of the compressibility of air and the substantial difference in wave impedance between air and liquid, these air layers can effectively attenuate HRAM loads[4−5].

It is generally recognized that the HRAM effect resulting from projectile water entry can be divided into

Received date：2025−08−06
Foundation items：Supported by the National Natural Science Foundation of China (52271338; 51979277; 52371342)
Biography：WU Meng-meng (1991−), female, Ph.D., candidate, lecturer, E-mail: mengmegnwu1017@163.com.
HOU Hai-liang(1977−), male, Ph.D., professor, corresponding author, E-mail: hou9611104@163.com;

four stages[6−7]: shock, drag, cavitation, and exit. These stages generate four characteristic pressures[8−9]: initial shock pressure wave, ballistic pressure at the projectile nose, drag pressure, and cavitation collapse pressure[10]. David et al[11] visualized the propagation process of the initial shock pressure wave generated during the shock stage using HRAM experiments, and analyzed the relationship between the projectile velocity and the intensity and propagation distance of the shock pressure wave. McMillen et al[12−13] used shadowgraphy to study the characteristics of shock pressure waves generated by high-speed projectile water entry, and analyzed the attenuation pattern of peak pressure with respect to distance and angle. They found that the intensity of shock pressure wave along the wavefront direction attenuates according to the relation $P = P_{90}\sin(\theta-7°)$, where P_{90} is the pressure in the ballistic direction and θ is the angle between pressure measurement point and liquid surface. However, Disimile et al[14] found that the attenuation relation of shock pressure wave along wavefront direction was $P = P_{90}\sin(\theta + 7°)$. While the experimental results of Zhang et al[15] fell between the two. This discrepancy is attributed to the presence of front wall plate, which increases the angular attenuation rate and thereby enhances the amplitude in the ballistic direction[16]. Chen[17] and Zhao[18] used the mirror theory and shadowgraphy to visualize the propagation and reflection processes of shock pressure wave, qualitatively analyzing that the pressure wave exhibits its highest strength at the initial stage, with both its intensity and propagation velocity gradually decreasing over time.

Based on the potential flow theory (assuming the fluid to be inviscid, incompressible, and irrotational), Logvinovich[19] simplified the Navier-Stokes equations and, combined with free surface boundary conditions and motion equations, derived a pressure distribution model for water entry. He also considered the effect of compressibility of water under high-speed impact on pressure wave propagation, providing a theoretical basis for calculating shock pressure waves during projectile water entry. On this basis, Lee et al[20] proposed analytical models for shock pressure waves of subsonic and supersonic projectiles penetrating into an infinite water domain. Liu et al[21] further revised Lee's model through numerical calculations by introducing a more reasonable distribution of point source strength, and validated the new model through spherical projectile penetration tests in a square tube. However, these pressure analysis largely overlooked the influence of wave reflection from finite structural boundaries, particularly the propagation and reflection of shock pressure waves between media with differing wave impedances.

As research into shock pressure waves generated by projectile water entry has progressed, researchers have proposed specific methods to effectively suppress or attenuate the strength of initial shock pressure waves by presetting the air layer to preserve the integrity of liquid-filled structure. Varas et al[22] conducted experiments on liquid-filled aluminum square tubes with varying fill levels. They found that a lower free surface leads to a shorter duration of positive pressure. Townsend et al[23] introduced thin air baffles and compressed air bubbles within the liquid-filled structure to disrupt and disperse the initial shock wave pressure, there by reducing the loads and damage on the liquid-filled structure by utilizing the difference in wave impedance between the air and liquid. Jin et al[4] proposed a method of presetting a spherical air bubble inside the liquid-filled structure. The compressibility of the air bubble can reflect rarefaction waves, and alter the flow field pressure environment. This effectively alleviates structural damage to the liquid-filled structure caused by shock pressure waves. Wu et al[5] experimentally studied the influence of different air layer configurations on the strength of shock pressure waves within the liquid-filled structure and found that a spherical air layer can significantly attenuate the strength of shock pressure waves and the duration of positive pressure.

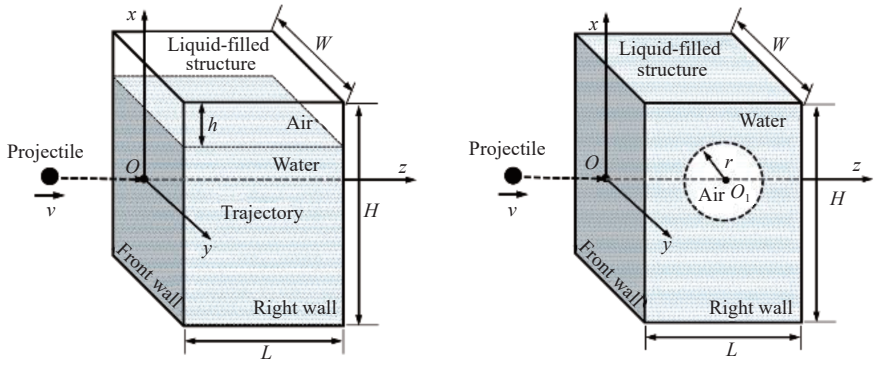
In summary, considerable progress has been made in the study of shock pressure waves generated by projectile water entry, primarily focusing on the generation mechanisms, influencing factors, strength, and

decay laws of shock pressure waves. However, the influence of a preset air layer in the liquid-filled structure on the propagation and strength of shock pressure waves remains to be further studied. To analyze the effect of preset air layer on the propagation and attenuation of shock pressure waves in the liquid-filled structure, this study establishes a computational model for the pressure wave considering reflection from a preset air layer. The model combines virtual and real mirror methods with potential flow theory. Its validity is verified through numerical simulations. Furthermore, the effects of top air layer's height, and the spherical air layer's center location and radius on pressure wave strength and propagation are analyzed.

1 Analysis model

1.1 Basic assumptions

As illustrated in Fig.1, the liquid-filled structure is defined by height (H), length (L), and width (W). The center of the front plate is impacted by a spherical projectile with diameter d, mass M_p, and initial velocity v_0. To analyze the attenuation effect of the air layer on pressure waves, two configurations are considered: an air layer of height (h) placed at the top of the liquid-filled structure (see Fig.1(a)), and a spherical air layer of radius (r) located at the center of the liquid-filled structure (see Fig.1(b)).



(a) Top air layer　　(b) Spherical air layer

Fig.1 Schematic diagram of liquid-filled structure and preset air layer configurations

A Cartesian coordinate system $Oxyz$ is established with the projectile impact point O as the origin. The x, y, and z axes respectively align with the height, length, and width directions of the liquid-filled structure. To facilitate the analysis, the penetration process of the projectile through the front plate is not considered.The projectile is modeled as a rigid body with negligible deformation and trajectory deflection. The effects of fluid viscosity are ignored. All kinetic energy loss during penetration is converted into the kinetic and potential energy of the liquid. The velocity attenuation of the projectile within the air layer is neglected.

The pressure wave strength varies with the relative position between the pressure point and the projectile. A correction function for pressure wave $f(\beta)$[21] is introduced as follows

$$f(\beta)=\begin{cases}1, -\dfrac{\pi}{4}<\beta<\dfrac{\pi}{4}\\ \cos\left(\beta-\dfrac{\pi}{4}\right), \beta\geqslant\dfrac{\pi}{4}\ \text{or}\ \beta\leqslant-\dfrac{\pi}{4}\end{cases} \tag{1}$$

where β is the angle between the line connecting the pressure point and projectile and the direction of projectile motion, as shown in Fig.2.

1.2 Pressure wave analysis with top air layer

When the liquid-filled structure is filled with liquid, due to the limited space of the structure, the pressure wave generated by the projectile penetrating the liquid is reflected as a compression wave at the structural wall and propagates back into the liquid, thereby increasing the liquid pressure. The reflection of the pressure wave at the structure wall follows the principle of mirror reflection.

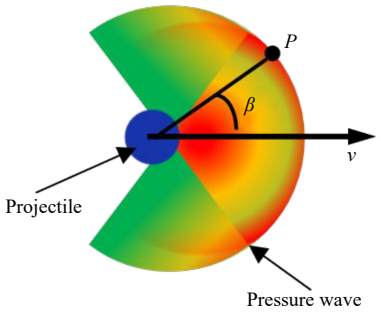
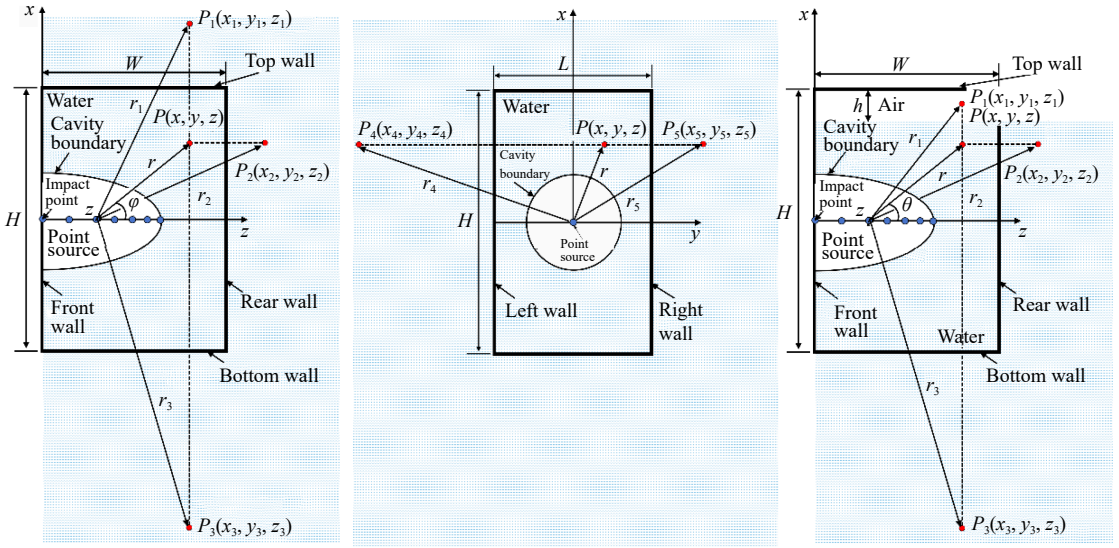


Fig.2 Schematic diagram of angular attenuation of pressure wave strength along the wavefront

For any pressure point $P(x, y, z)$ inside the liquid-filled structure, the mirror points of P with respect to the top wall, rear wall, bottom wall, and the left and right walls of the structure are $P_1(H-x, y, z)$, $P_2(x, y, 2W-z)$, $P_3(-(H+x), y, z)$, $P_4(x, -(L+y), z)$ and $P_5(x, L-y, z)$, respectively, as shown in Fig.3. The pressure at point P can be calculated by superimposing the pressure $p_0(t)$ at P in the infinite field and the pressure $p_i(t)$ at its mirror points P_1 to P_5 (where $i = 1,\cdots,5$), that is

$$p(t) = \sum p_i(t) + p_0(t) \tag{2}$$



(a) Fully filled (b) Top air layer

Fig.3 Mirror process of pressure points and pressure wave analysis model

The motion of the projectile during the penetration of the liquid can be regarded as a moving point source[20], as shown in Fig.3. According to potential flow theory and the Bernoulli equation, the intensity of the pressure wave at any point p_i in the flow field is expressed as [20−21], where $i = 0,1,\cdots,5$

$$p_i(t) = p_0 - \rho_w \frac{\partial \varphi}{\partial t} - \frac{1}{2}\rho_w u^2 \tag{3}$$

where the fluid potential energy is

$$\varphi(x_i, y_i, z_i, t) = -\int_0^{z_{p_i}(t)} \frac{S(\xi, t - r_i/c)}{r} \mathrm{d}\xi \tag{4}$$

where u is the velocity of the liquid at the pressure point, p_0 is the atmospheric pressure, ρ_w is the density of water, $\frac{\partial \varphi}{\partial t}$ is the instantaneous rate of change of fluid potential at a fixed point in space, ξ denotes the motion direction of the projectile, r_i is the distance from the point source to the pressure point p_i,

$r_i = \sqrt{x_i^2 + y_i^2 + (z_i - z_{p_i})^2}$, z_{p_i} is the position of the projectile in the ξ direction when the pressure wave reaches point P_i, S represents the strength of the point source, which depends on ξ, t is the time when the pressure point receives the pressure wave generated by the projectile impact, $t-r/c$ is the time of projectile motion, $z_p(t)$ is the position of the projectile.

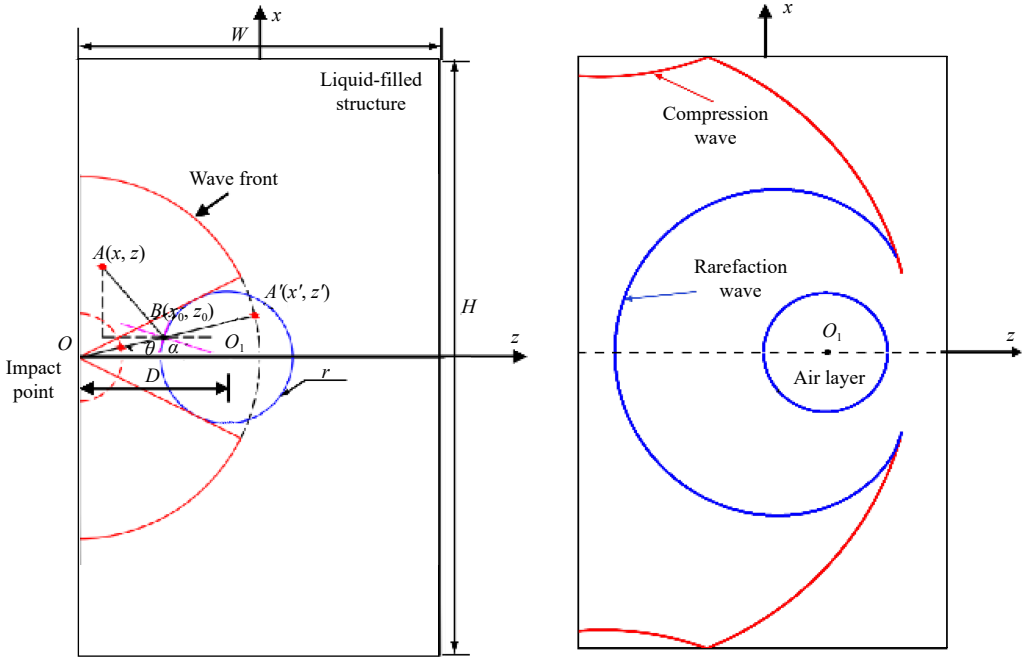
When an air layer is preset at the top of the liquid-filled structure (see Fig.1(a)), the pressure wave generated by the projectile entering the water will reflect a rarefaction wave at the air-liquid interface and propagate into the liquid. Since the liquid is incompressible, when the rarefaction wave reaches the pressure point P, the pressure at this point rapidly drops to the ambient pressure, resulting in a truncation effect [24]. Then, the mirror point of P relative to the free surface is $P_1(H-2h-x, y, z)$, while the coordinates of the mirror points relative to other walls remain unchanged. If the compression wave reflected from the structure wall reaches point P before the rarefaction wave, a multi-wave superposition effect may occur. However, once the rarefaction wave arrives, the pressure at P drops sharply to the ambient pressure. Conversely, under the influence of the low-pressure effect induced by the rarefaction wave, the impact of the compression wave reflected from the wall on the pressure can be neglected. That is

$$p(t) = \begin{cases} \sum p_i(t), 0 < t < t_1 \\ 0, t > t_1 \end{cases} \quad (i = 0, 1, \cdots, 5) \tag{5}$$

where t_1 is the time at which the rarefaction wave reaches point P, and it can be calculated based on the coordinates of P_1.

1.3 Pressure wave analysis with a spherical air layer

A spherical air layer with radius r is preset on the projectile's trajectory, and the center of the sphere O_1 is at a distance D from the impact point O, as shown in Fig.4(a). In order to determine the position of the wavefront at any given moment as the pressure wave propagates within the liquid-filled structure containing a spherical air layer, the continuous wavefront is discretized into a finite number of particles[17]. Assume the average propagation velocity of the pressure wave in water is c. Each particle on the wavefront travels at



(a) Parameter definition　　(b) Pressure wave reflection

Fig.4 Schematic diagram of pressure wave reflection from a spherical air layer

velocity c from the impact point into the surrounding liquid. When the particle path intersects the air layer interface, it is reflected as a rarefaction wave; otherwise, the particle continues to move with the wavefront. Meanwhile, when the particle reaches the structure walls, the path of the reflected compression wave is consistent with that shown in Fig.4.

In order to analyze the position of a particle on the pressure wavefront within the air-layered liquid-filled structure at any moment, the propagation of a particle A on the symmetric plane xoz is taken as the object of study. At any moment t, the motion distance of point A, i.e., the radius of the wavefront, is $R=c\cdot t$. Let the actual coordinates of particle A be (x, z). If particle A passes through the air layer without reflection, it will propagate with the pressure wavefront to point A', with coordinates (x', z'). The angle between OA' and the x-axis is θ, and the coordinates of the intersection point B between OA' and the air layer are (x_0, z_0). The angle between O_1B and the z-axis is α.

When $R < D\text{-}r$, or $R \geqslant D\text{-}r$ and $\arcsin\dfrac{r}{D} < |\theta| < 90°$, the pressure wave does not interact with the air layer, and the coordinates of point A can be expressed as

$$\begin{cases} x = R\cos\theta \\ z = R\sin\theta \end{cases} \tag{6}$$

When $R \geqslant D\text{-}r$ and $-\arcsin\dfrac{r}{D} < \theta < \arcsin\dfrac{r}{D}$, based on the geometric relationships in Fig.4(a), we can obtain the coordinates of points A' and B

$$\begin{cases} x' = R\cos\theta \\ z' = R\sin\theta \end{cases} \tag{7}$$

$$\begin{cases} x_0 = z_0\tan\theta \\ z_0 = \dfrac{r\sin\alpha}{\sin\theta\sqrt{1+\tan^2\theta}} \end{cases}, \left(-\arcsin\frac{r}{D} < \theta < \arcsin\frac{r}{D}\right) \tag{8}$$

According to the Eqs. (7)-(8), the coordinate of point A reflected from the air layer is

$$\begin{cases} x = x_0 + \left(R - \sqrt{z_0^2 + x_0^2}\right)\sin(2\alpha+\theta) \\ z = z_0 - \left(R - \sqrt{z_0^2 + x_0^2}\right)\cos(2\alpha+\theta) \\ \sin\alpha = \dfrac{z_0\tan\theta}{r} \end{cases} \tag{9}$$

In the above equations, the range of θ is [−90°, 90°]. Based on Eqs. (6) and (9), the propagation process of the rarefaction wavefront reflected by the air layer can be plotted (see Fig.4(b)), which can be used to determine the time at which the rarefaction wave reaches the pressure point. As shown in Fig.4(b), the rarefaction wave reflected from the air layer propagates spherically immediately following the initial pressure wave, causing the compression wave reflected from the structure wall to be truncated by the rarefaction wave. Therefore, when a spherical air layer is present, the analysis of the pressure wave only considers the compression wave reflected from the rear wall generated by the projectile's secondary water entry.

To analyze the pressure wave intensity at point P, the projectile's motion in the liquid is divided into three stages, as illustrated in Fig.5. Stage I is the initial water entry, Stage II is the

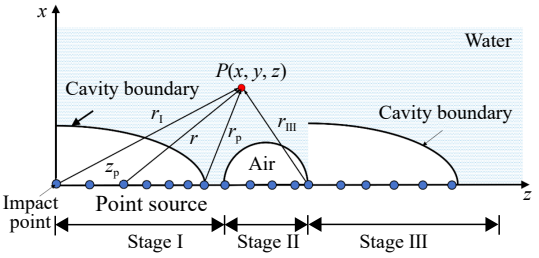


Fig.5 Schematic diagram of projectile penetration in a liquid-filled structure with a preset spherical air layer

penetration through the air layer, and Stage III is the secondary water entry. The air resistance encountered by the projectile during Stage II can be neglected, and its kinetic energy can be assumed to remain unchanged.According to the law of conservation of energy, the contributions of the three zones in Fig.5 to the pressure wave are divided into the following time segments:

(1) $0 < t < t_{\mathrm{I}}$. During Stage I, the pressure wave at the pressure point is generated by the kinetic energy loss of the projectile during this stage. t_{I} is the time when the projectile penetrates into the air layer.

(2) $t_{\mathrm{I}} < t < t_{\mathrm{II}}$. During Stage II, the projectile penetrates the air layer. Since there is no kinetic energy loss while the projectile travels through the air layer, no pressure wave is generated during this stage.

(3) $t_{\mathrm{II}} < t < t_{\mathrm{III}}$. During Stage III, the projectile exits the air layer and reenters water. The pressure wave at the pressure point is generated by the kinetic energy loss of the projectile during this stage.

During the projectile's penetration of the liquid-filled structure, its velocity attenuation and displacement in the liquid can be expressed by stages as follows[5]

$$\begin{cases} v_{\mathrm{pI}} = \dfrac{v_0}{1+\beta v_0 t}, & t \leqslant t_{\mathrm{I}} \\ v_{\mathrm{pII}} = \mathrm{Const}, & t_{\mathrm{I}} < t \leqslant t_{\mathrm{II}} \\ v_{\mathrm{pIII}} = \dfrac{v_{\mathrm{pII}}}{1+\beta v_{\mathrm{pII}}(t-t_{\mathrm{II}})}, & t_{\mathrm{II}} < t \leqslant t_{\mathrm{III}} \end{cases} \tag{10}$$

$$\begin{cases} z_{\mathrm{pI}} = \dfrac{1}{\beta}\ln(v_0\beta t+1), & t \leqslant t_{\mathrm{I}} \\ z_{\mathrm{pII}} = v_{\mathrm{pII}}(t-t_{\mathrm{I}}) + z_{\mathrm{pI}}, & t_{\mathrm{I}} < t \leqslant t_{\mathrm{II}} \\ z_{\mathrm{pIII}} = z_{\mathrm{pII}} + \dfrac{1}{\beta}\ln(v_{\mathrm{pIII}}\beta(t-t_{\mathrm{II}})+1), & t_{\mathrm{II}} < t \leqslant t_{\mathrm{III}} \end{cases} \tag{11}$$

$$\beta = \frac{\rho_w A_0 C_{\mathrm{d}}}{2M_{\mathrm{p}}} \tag{12}$$

where M_{p} is the mass of the projectile, v_{p} is the instantaneous velocity of the projectile in water, z_{p} is the penetration displacement of the projectile in the liquid, A_0 is the projected area of the projectile in the direction opposite to penetration, C_{d} is the drag coefficient of the projectile in water, which is taken as 0.4 for a spherical projectile entering water at low speed. t_{I} is the time when the projectile enters the air bubble, t_{II} is the time when the projectile exits the air bubble and reenters water, t_{III} is the time when the projectile reaches the rear wall plate. v_{pI} and z_{pI} are the velocity and position of the projectile in Stage I, v_{pII} and z_{pII} are the velocity and position of the projectile in Stage II, and v_{pIII} and z_{pIII} are the velocity and position of the projectile in Stage III.

From Eqs. (10) and (11), the attenuation rate of the projectile's kinetic energy with respect to penetration displacement can be obtained as

$$\begin{cases} \dfrac{\mathrm{d}E_{\mathrm{pI}}}{\mathrm{d}z_{\mathrm{pI}}} = m_{\mathrm{p}}\beta v_{\mathrm{pI}}^2, & 0 \leqslant t \leqslant t_{\mathrm{I}} \\ \dfrac{\mathrm{d}E_{\mathrm{pII}}}{\mathrm{d}z_{\mathrm{pII}}} = 0, & t_{\mathrm{I}} < t \leqslant t_{\mathrm{II}} \\ \dfrac{\mathrm{d}E_{\mathrm{pIII}}}{\mathrm{d}z_{\mathrm{pIII}}} = m_{\mathrm{p}}\beta v_{\mathrm{pIII}}^2, & t_{\mathrm{II}} < t \leqslant t_{\mathrm{III}} \end{cases} \tag{13}$$

Therefore, the instantaneous rate $\dfrac{\partial \varphi}{\partial t}$ of change of the fluid potential energy with respect to time in Eq.(1) can be expressed piecewise as

$$\frac{\partial \varphi}{\partial t}=\begin{cases}-\dfrac{1}{2}\dfrac{BA}{r_{\mathrm{p}}}\dfrac{v_{\mathrm{p}}}{1-\dfrac{v_{\mathrm{p}}}{c}\dfrac{z-z_{\mathrm{p}}}{r_{\mathrm{p}}}}+\dfrac{1}{2}B^{2}\ln\left[\dfrac{z+r_{\mathrm{I}}}{z-z_{\mathrm{p}}+r_{\mathrm{p}}}\right], & 0<t\leqslant t_{\mathrm{I}}\\ -\dfrac{1}{2}\dfrac{BA}{r_{\mathrm{p}}}\dfrac{v_{\mathrm{p}}}{1-\dfrac{v_{\mathrm{p}}}{c}\dfrac{z-z_{\mathrm{p}}}{r_{\mathrm{p}}}}+\dfrac{1}{2}B^{2}\ln\left[\dfrac{z+r_{\mathrm{III}}}{z-z_{\mathrm{p}}+r_{\mathrm{p}}}\right], & t_{\mathrm{II}}<t<t_{\mathrm{III}}\end{cases}\tag{14}$$

The velocity of the liquid at the pressure measurement point in the z direction and the x or y direction can be expressed piecewise as

$$u_z=\frac{\partial \varphi}{\partial z}=\begin{cases}\dfrac{BA}{r_{\mathrm{p}}}\dfrac{\dfrac{v_{\mathrm{p}}}{c}\dfrac{z-z_{\mathrm{p}}}{r_{\mathrm{p}}}}{1-\dfrac{v_{\mathrm{p}}}{c}\dfrac{z-z_{\mathrm{p}}}{r_{\mathrm{p}}}}+\dfrac{1}{2}B\displaystyle\int_{0}^{z_b(t)}\left\{A(\xi)-B[t-t_{\mathrm{p}}(\xi)]\frac{z-\xi}{{r_0}^{3}}\right\}\mathrm{d}\xi, & 0<t\leqslant t_{\mathrm{I}}\\ \dfrac{BA}{r_{\mathrm{p}}}\dfrac{\dfrac{v_{\mathrm{p}}}{c}\dfrac{z-z_{\mathrm{p}}}{r_{\mathrm{p}}}}{1-\dfrac{v_{\mathrm{p}}}{c}\dfrac{z-z_{\mathrm{p}}}{r_{\mathrm{p}}}}+\dfrac{1}{2}B\displaystyle\int_{t(z_{\mathrm{pII}})}^{z_b(t)}\left\{A(\xi)-B[t-t_{\mathrm{p}}(\xi)]\frac{z-\xi}{{r_0}^{3}}\right\}\mathrm{d}\xi, & t_{\mathrm{II}}<t<t_{\mathrm{III}}\end{cases}\tag{15}$$

$$u_x=\frac{\partial \varphi}{\partial x}=\begin{cases}\dfrac{BA}{r_{\mathrm{p}}}\dfrac{\dfrac{v_{\mathrm{p}}}{c}\dfrac{x}{r_{\mathrm{p}}}}{1-\dfrac{v_{\mathrm{p}}}{c}\dfrac{z-z_{\mathrm{p}}}{r_{\mathrm{p}}}}+\dfrac{1}{2}Bx\displaystyle\int_{0}^{z_b(t)}\{A(\xi)-B[t-t_{\mathrm{p}}(\xi)]\}\frac{1}{{r_0}^{3}}\mathrm{d}\xi, & 0<t\leqslant t_{\mathrm{I}}\\ \dfrac{BA}{r_{\mathrm{p}}}\dfrac{\dfrac{v_{\mathrm{p}}}{c}\dfrac{x}{r_{\mathrm{p}}}}{1-\dfrac{v_{\mathrm{p}}}{c}\dfrac{z-z_{\mathrm{p}}}{r_{\mathrm{p}}}}+\dfrac{1}{2}Bx\displaystyle\int_{t(z_{\mathrm{pII}})}^{z_b(t)}\{A(\xi)-B[t-t_{\mathrm{p}}(\xi)]\}\frac{1}{{r_0}^{3}}\mathrm{d}\xi, & t_{\mathrm{II}}<t<t_{\mathrm{III}}\end{cases}\tag{16}$$

$$A=\sqrt{\frac{\mathrm{d}E_{\mathrm{p}}/\mathrm{d}z_{\mathrm{p}}}{\pi(p_0-p_c)}},\quad B=\sqrt{\frac{p_0-p_c}{\rho_{\mathrm{w}}N}}\tag{17}$$

In Eqs. (14)-(17), z_{p} and v_{p} represent the projectile's displacement and velocity, r is the distance from the pressure measurement point to the point source, r_{p} is the distance from the projectile at position z_{p} to the pressure measurement point, p_{c} is the cavitation pressure (taken as the vapor pressure of the liquid at room temperature), A_{p} is the value of A when the projectile is at position z_{p}, z is the z-coordinate of the pressure measurement point, B is a constant, N is the kinetic energy compensation coefficient[25], its value is 1[26–27], and $\mathrm{d}E_{\mathrm{p}}/\mathrm{d}z_{\mathrm{p}}$ is the rate of change of the projectile's kinetic energy with respect to its displacement. $r_{\mathrm{I(III)}}$ is the distance between the projectile and the pressure measurement point at the moment of water entry in Stage I and Stage III. By substituting Eqs. (10)-(17) into Eq.(5), the pressure wave intensity at any point in the liquid can be calculated when a spherical air layer is preset in the liquid-filled structure.

From the analysis above, when a spherical air layer is preset on the projectile trajectory, the projectile reenters water after passing through the air layer and generates a secondary pressure wave. According to the propagation characteristics of the pressure wave, the impact zones of the initial and secondary pressure waves can be divided as shown in Fig.6. Zone I is the area affected by the initial pressure wave, bounded by the tangent line from the projectile's impact point to the air layer. Due to

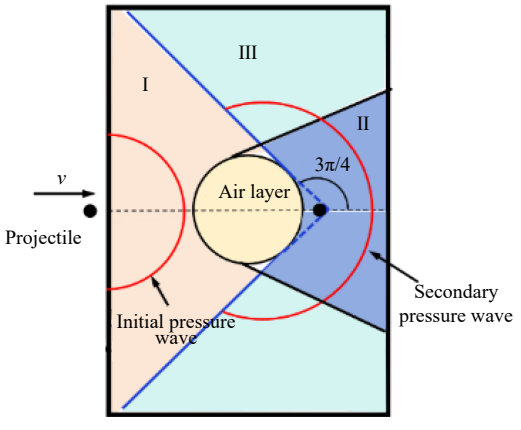


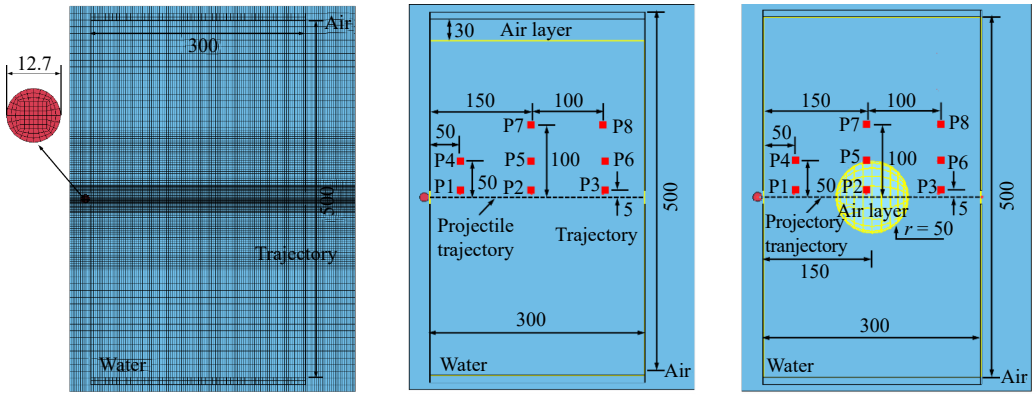
Fig.6 Schematic diagram of pressure wave zone division

the large wave impedance between air and liquid, the air layer blocks the initial pressure wave from propagating beyond it. Zone II is the secondary pressure wave zone. According to Eq.(1), the intensity of the pressure wave varies with the circumferential angle β. The maximum extent of this zone occurs following the projectile's secondary water entry, located within the tangent lines of the air layer when β equals $3\pi/4$. Zone III is the interaction zone of both initial and secondary pressure waves.

2 Numerical calculation

2.1 Finite element model

To verify the accuracy of the above analysis model, numerical simulations of a projectile penetrating a liquid-filled structure are conducted using the explicit dynamic analysis software LS-DYNA. The dimensions of the liquid-filled structure are illustrated in Fig.1, with a height of 500 mm, a width of 300 mm, and a length of 340 mm. All sides of the structure are enclosed with rigid steel plates. The projectile is a spherical tungsten alloy body with a diameter of 12.7 mm and a mass of 19.1 g. To minimize velocity attenuation due to interaction with the front and rear walls, circular openings with a diameter of 18 mm were pre-cut at the centers of both walls. The projectile enters the structure through the front hole with an initial velocity of $v_0=450$ m/s. The height of the air layer at the top is 30 mm, and the radius of the spherical air layer on the trajectory is 50 mm, with its center located 150 mm from the front wall. A half-symmetry model is adopted, as shown in Fig.7(a). A gradient mesh is applied, with mesh refinement along the projectile's penetration trajectory. Specifically, a fine mesh of $1\times1\times1$ mm^3 is used within 0-100 mm from the projectile trajectory, a medium transitional mesh of $3\times3\times3$ mm^3 is used for the 100-200 mm region, and a coarse mesh of $5\times5\times5$ mm^3 is applied elsewhere. The preset air layer is introduced using an initialization command.



(a) Mesh division　(b) Top air layer　(c) Spherical air layer

Fig.7 Finite element model and pressure point locations (unit: mm)

Eight pressure points are selected at different distances from the projectile trajectory in the key area covering the propagation of the pressure wave to conduct pressure time history analysis (see Fig.7), and to enable comparison between the measurement results and those from the analysis model.

Both the air outside the liquid-filled structure and the internal preset air layer are modeled as ideal gases, and is described by a Linear Polynomial Equation of State

$$P=C_0+C_1\mu+C_2\mu^2+C_3\mu^3+(C_4+C_5\mu+C_6\mu^2)E \tag{18}$$

where μ is the compressibility, $\mu=\rho/\rho_0-1$, ρ and ρ_0 are the instantaneous and initial densities of the medium, respectively. E is the internal energy per unit volume, and C_0-C_6 are constants. For an ideal gas, $C_0=C_1=$

$C_2=C_3=C_6=0$, $C_4=C_5=\gamma$-1, and the specific heat ratio γ is set to 1.4. The initial internal energy per unit volume of air at standard conditions is $E_0=253.3$ kJ/m^3.

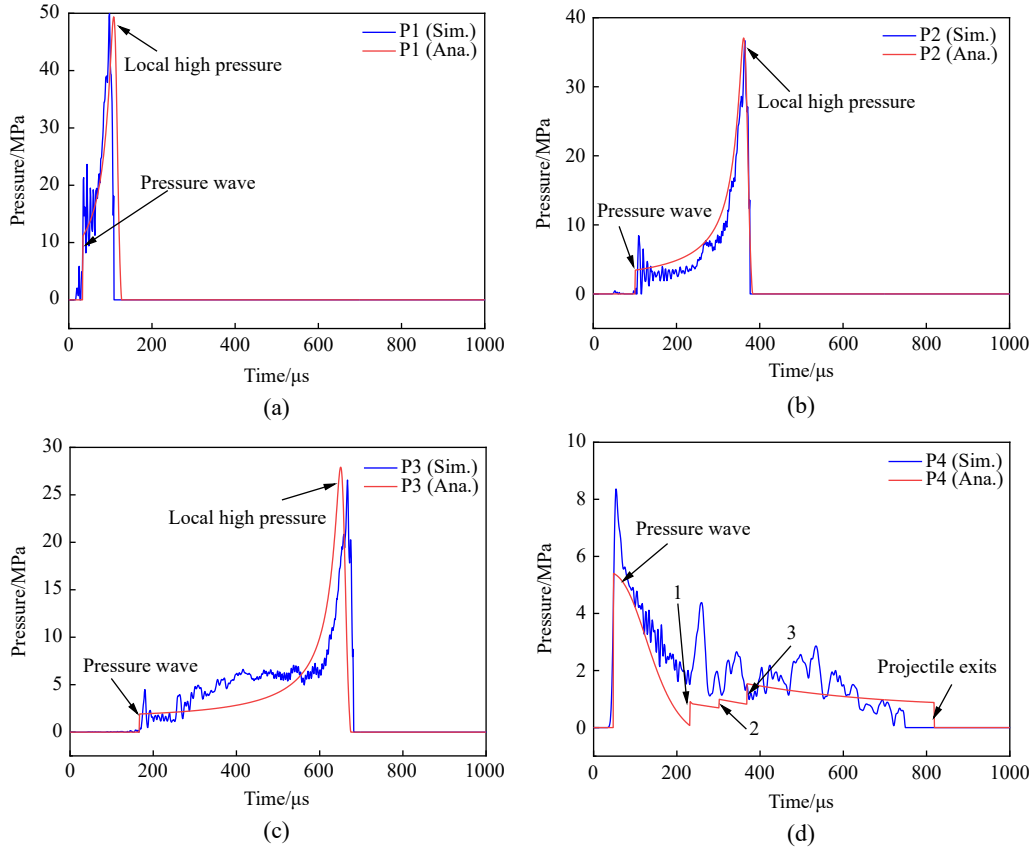
Water is assumed to be a compressible, inviscid, and irrotational fluid. Its behavior is represented by the Grüneisen equation of state

$$P=\frac{\rho_0 c^2\mu[1+(1-\gamma_0/2)\mu-a\mu^2/2]}{[1-(S_1-1)\mu-S_2\mu^2/(\mu+1)-S_3\mu^2/(\mu+1)^2]^2}+(\gamma_0+a\mu)E \tag{19}$$

where pressure wave velocity in water is set to 1484 m/s, the Grüneisen parameter γ_0 is 0.11, and the first-order volume correction α of γ_0 and μ is 3, S_1, S_2, and S_3 are curve-fitting parameters, with S_1 = 1.979, and S_2 = S_3 = 0. The initial internal energy per unit volume of water E_0 is set to 921.1 kJ/m^3, and the initial density ρ_0 is set to 1000 kg/m^3. Structure walls and the projectile are modeled as rigid bodies.

2.2 Verification of pressure wave analysis results

Figs.8-10 present the pressure time history curves at each pressure point within the liquid-filled structure under three different working conditions: fully filled with liquid, with a top air layer, and with a spherical air layer. It can be seen from the figures that, after taking into account the compression waves reflected from the rigid walls and the rarefaction waves reflected from the air layer interface, the pressure amplitude and waveform of the pressure time history curves obtained from both the analytical and numerical methods show good agreement. For P1-P3, which are closest to the projectile trajectory, the average relative error of peak pressure is 2%. For P4-P6, which are at an intermediate distance, the average relative errors of peak pressure are 15.8% (fully filled), 13.9% (with top air layer), and 15.9% (with spherical air layer), respectively. For the furthest points P7-P8, the average relative errors of peak pressure are 10.5%, 12.3%, and 24% under the same three conditions. The above comparison results confirm the correctness of the proposed analysis model.



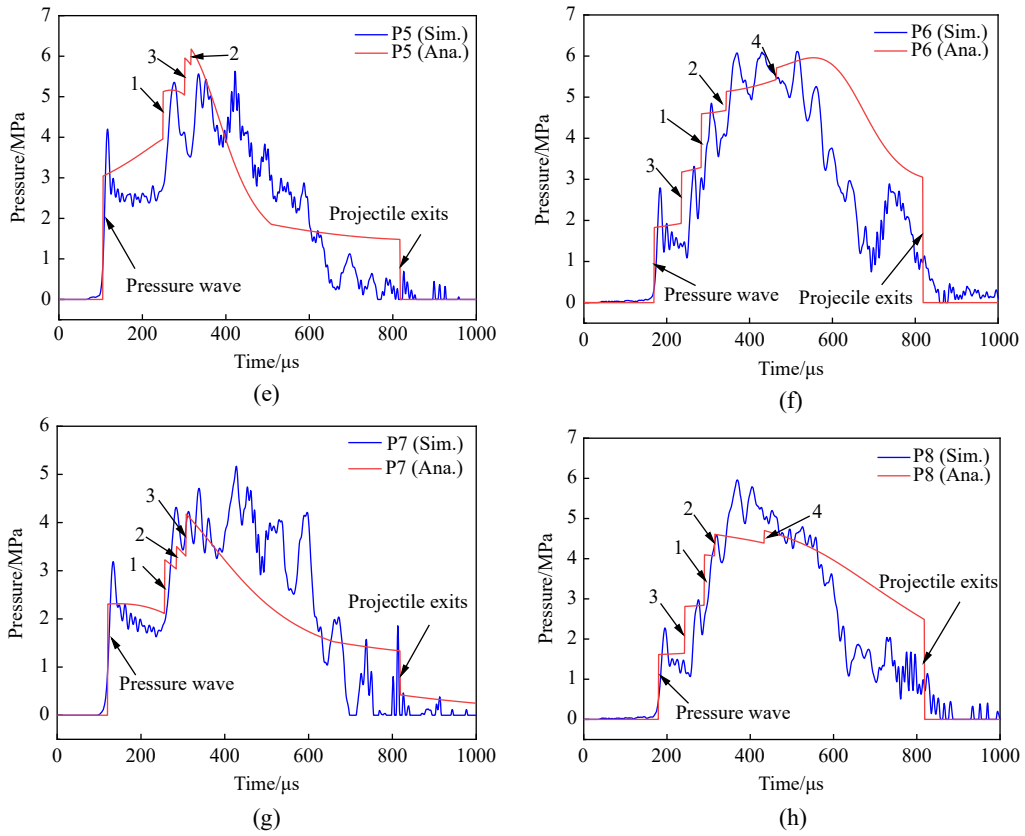
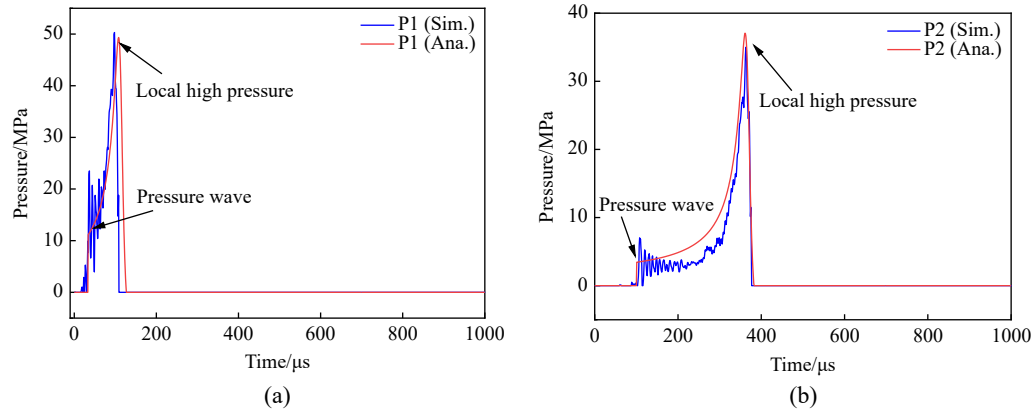


Fig.8 Comparison of pressure time history curves at different points under fully filled condition (1: Compression wave reflected from the left and right walls, 2: Compression wave reflected from the top wall, 3: Compression wave reflected from the rear wall, 4: Compression wave reflected from the bottom wall)

Comparison of the pressure time history curves at P1-P3 (Figs.8(a)-(c), 9(a)-(c), and 10(a)-(b)) shows that the pressure at the points close to the projectile trajectory is mainly dominated by the pressure wave and the transient local high pressure at the projectile nose. Due to cavitation effects induced by the high-speed motion of the projectile, these points enter the cavitation zone before the rarefaction wave reflected from the air layer reaches them, resulting in a rapid pressure drop to ambient pressure without being affected by the rarefaction wave. Comparison of the pressure history curves at P4-P8 (Figs.8(d)-(h), 9(d)-(h)) shows that when the compression waves reflected from the structure's walls reach a point before the rarefaction wave, a multi-wave superposition effect occurs. However, once the rarefaction wave arrives, the pressure drops sharply to ambient pressure, producing a truncation effect, as described by Eq.(5). Conversely, when the



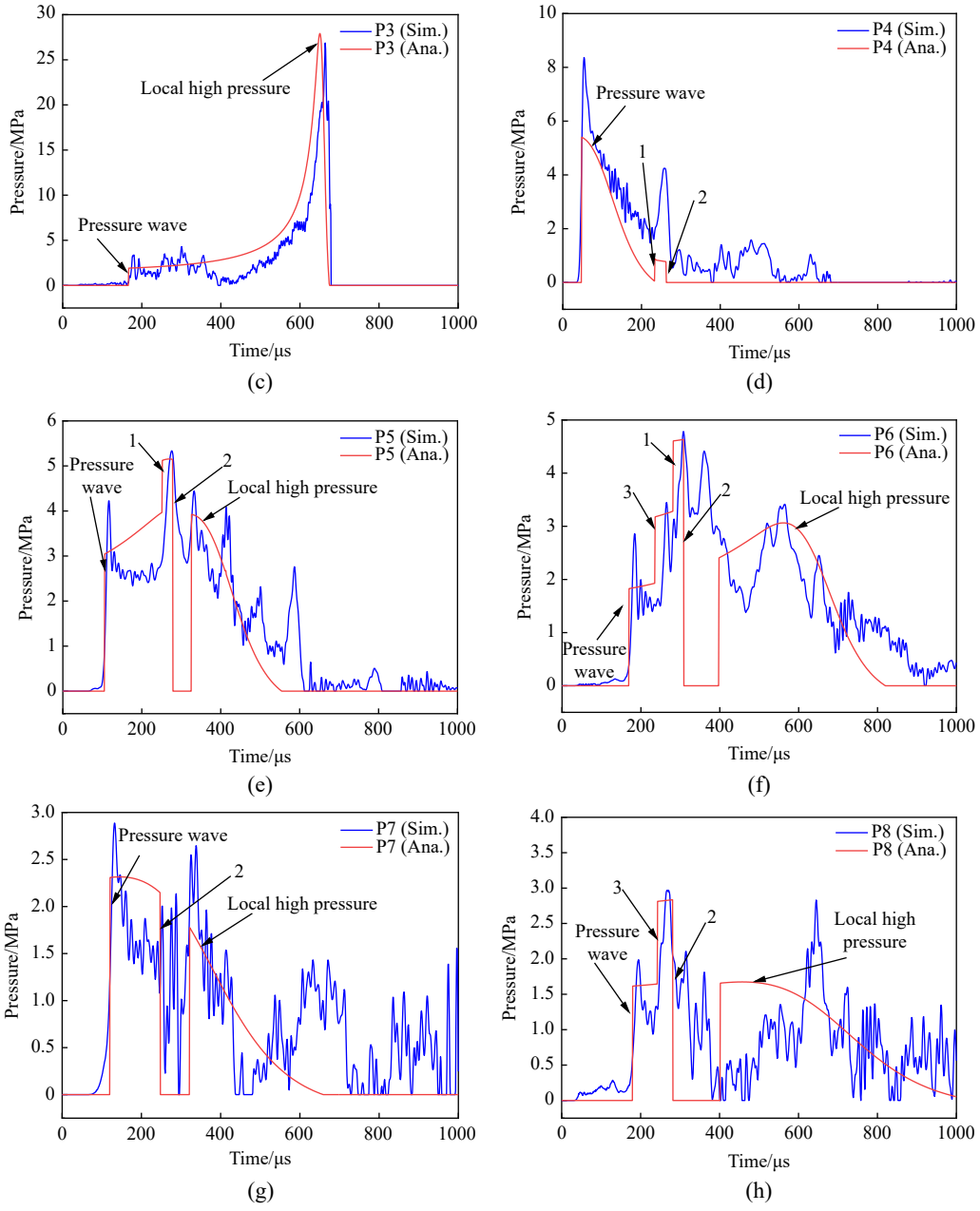


Fig.9 Comparison of pressure time history curves at different points with free surface at the top (1: Compression wave reflected from the left and right walls, 2: Truncation effect caused by rarefaction wave reflects from the free surface, 3: Compression wave reflected from the rear wall)

rarefaction wave reflected from the air layer arrives at the point earlier than the compression wave reflected from the rigid walls, the low-pressure effect induced by the rarefaction wave suppresses the wall-reflected compression wave.

As shown in Fig.10, when a spherical air layer with a radius of 50 mm is preset on the projectile trajectory, the pressure time history curve of P4, which is located in pressure wave Zone I (Fig.6), indicates that the pressure at this point is mainly from the initial pressure wave of the projectile (Fig.10(c)). At 63 μs, the rarefaction wave reflected from the air layer reaches the point, and the pressure rapidly drops to ambient pressure. Meanwhile, the rarefaction wave propagates into the liquid and blocks the compression wave reflected from the structure wall from affecting this point. As shown in Fig.10(d), the pressure at P6, which is

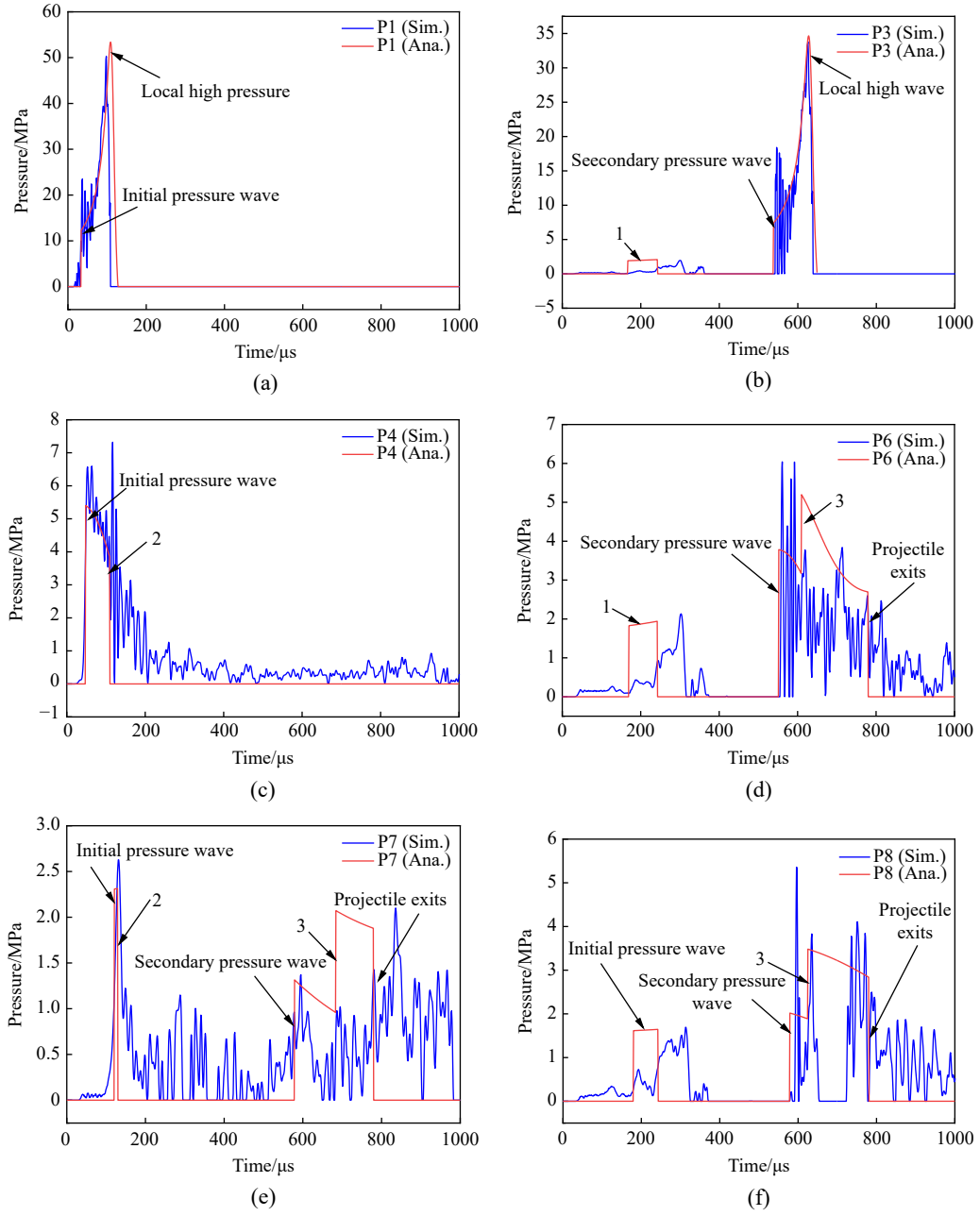


Fig.10 Comparison of pressure history curves at different points with spherical air layer (1: Disturbance pressure caused by the initial water entry, 2: Truncation effect caused by rarefaction wave reflects from the air layer, 3: Compression wave reflects from the rear wall)

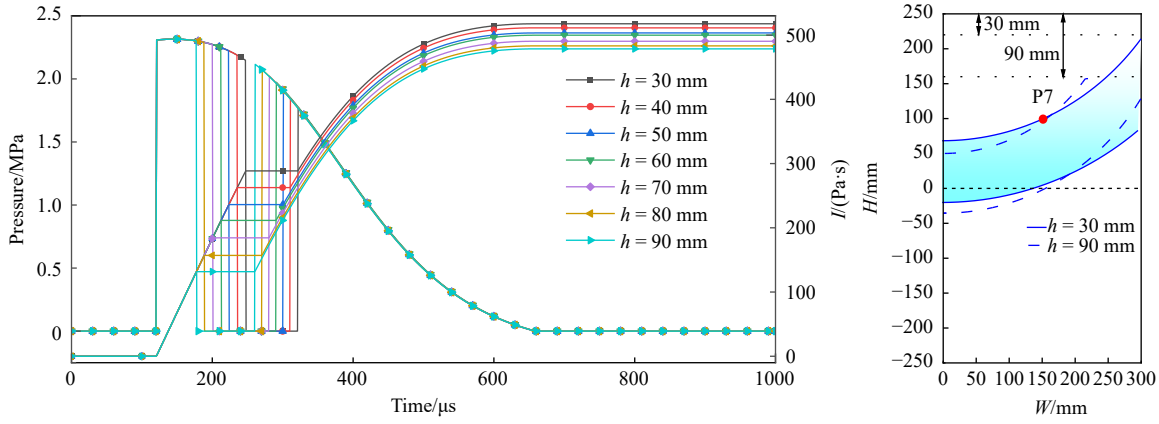
located in Zone II (Fig.6), is mainly due to the secondary pressure wave generated by the projectile's secondary water entry and its superposition with the compression wave reflected from the rear wall. The energy transferred to the liquid during the initial water entry also produces a minor pressure disturbance in this region, and the peak value of the initial pressure disturbance at P6 reaches 34% of the peak of the secondary pressure wave. At points P7 and P8 located in Zone III (Fig.6), as shown in Figs. 10(e) and 10(f), the pressure results from the superposition of the initial pressure wave, the secondary pressure wave from the second water entry, and the compression wave reflected from the rear wall. Taking P7 as an example, the initial pressure wave reaches this point at 120 μs, creating a pressure peak. 11 μs later, the rarefaction wave reflected from the air layer arrives and causes the pressure to drop to ambient. The projectile then exits the air

layer and reenters water, with the secondary pressure wave reaching P7 at 578 μs, producing another pressure peak. At 683 μs, the compression wave reflected from the rear wall arrives and causes pressure superposition. At 780 μs, the projectile exits the liquid-filled structure.

3 Analysis and discussion

3.1 Effect of free surface height on pressure wave

Since pressure points located close to the projectile trajectory are not affected by the rarefaction waves, point P7 in Fig.7 is selected to analyze the effect of the vertical distance h between the free surface and the top plate on the pressure wave (see Fig.11).The initial velocity of the projectile is 450 m/s. As shown in Fig.11(a), the increase in height h directly shortens the vertical distance from the air layer interface to P7, causing the rarefaction wave reflected from the air layer to reach P7 earlier and inducing a truncation effect. When $h=30$ mm, the rarefaction wave reaches 128 μs after the pressure wave. When $h=60$ mm, the rarefaction wave arrives after 94 μs. When $h=90$ mm, it arrives after 58 μs. The truncation time of pressure at P7 caused by the rarefaction wave is indicated by the blue region in Fig.11(b). After this point, pressure at P7 increases again due to continued interaction between the projectile and the liquid, generating additional pressure waves. Comparing the specific impulse at P7 under different h, it is found that when $h=60$ mm and $h=90$ mm, the specific impulse at P7 is 96.5% and 92.4% of that at $h=30$ mm, respectively. Therefore, the larger the h is, the more significant the attenuation effect of the rarefaction wave on the pressure wave is.



(a) History curves of pressure and specific impulse vs. h (b) Diagram of rarefaction wave inference region

Fig.11 Effect of vertical distance h (free surface to top plate) on pressure wave

3.2 Effect of spherical air layer position on pressure wave

To analyze the effect of the spherical air layer center position on the initial and secondary pressure waves, three pressure points P4, P6, and P7 in Fig.7 are selected to study the effect of the variation in distance D from the air center to the front wall. The corresponding wavefront of rarefaction waves reaching each pressure point are shown in Fig.12. The calculation conditions are the same as previously described.

As shown in Fig.12, point P4 in Zone I (see Fig.6) is only affected by the initial pressure wave. A smaller D causes the rarefaction wave to reach P4 earlier, shortening the duration of the positive pressure phase of the initial pressure wave. The maximum reduction in specific impulse reaches 87%. Point P6 in Zone II (see Fig.6) is primarily affected by the secondary water-entry pressure wave. A larger D increases the time required for the projectile to penetrate through the air layer and reenter water, delaying the arrival of the secondary pressure wave at P6 and reducing its peak pressure. The maximum attenuation rates of peak

pressure and specific impulse are 49.3% and 56.4%, respectively. Point P7 in Zone III (see Fig.6) is affected by both initial and secondary pressure waves. A smaller D results in a shorter duration of the initial pressure wave and a longer duration of the secondary pressure wave, thus increasing the specific impulse, conversely, a layer D has the oppsite effect. However, when $D=200$ mm, P7 falls into Zone I (see Fig.6), where the secondary pressure wave cannot effectively reach P7.

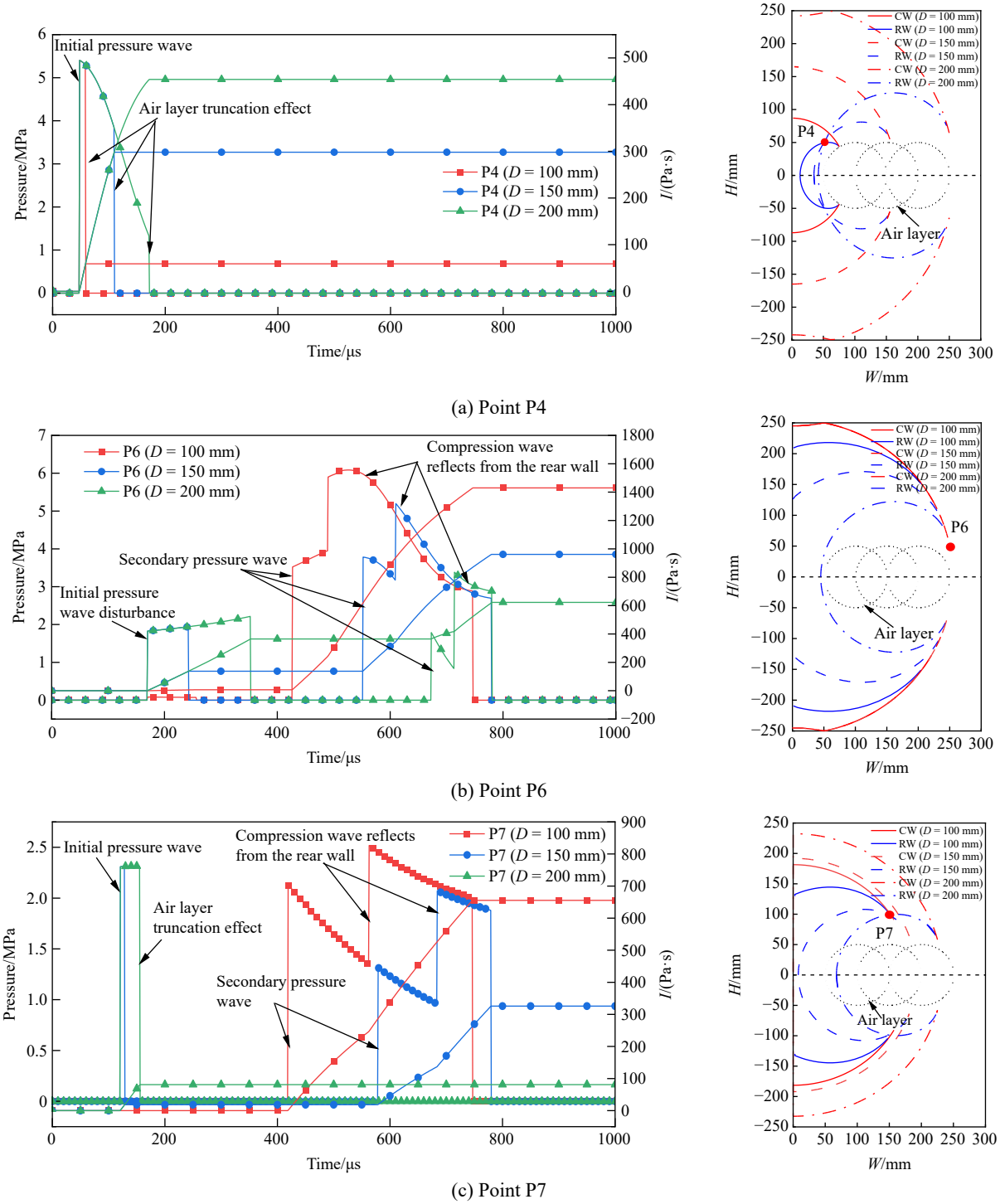


Fig.12 Time history curves of pressure and specific impulse vs. spherical center position D and propagation of rarefaction waves reflected from air layer interfaces (CW: compression wave, RW: rarefaction wave)

3.3 Effect of spherical air layer size on pressure wave

To analyze the effect of spherical air layer size on the initial and secondary water entry pressure waves, point P7 in Fig.7 is selected to study the effect of the variation in spherical air layer radius r (see Fig.13(a)). The distance D from the spherical center to the front wall is set to 150 mm, and the calculation conditions are the same as previously described. The schematic diagram of the wave fronts when the rarefaction waves reflected from different air layer sizes reach P7 is shown in Fig.13(b).

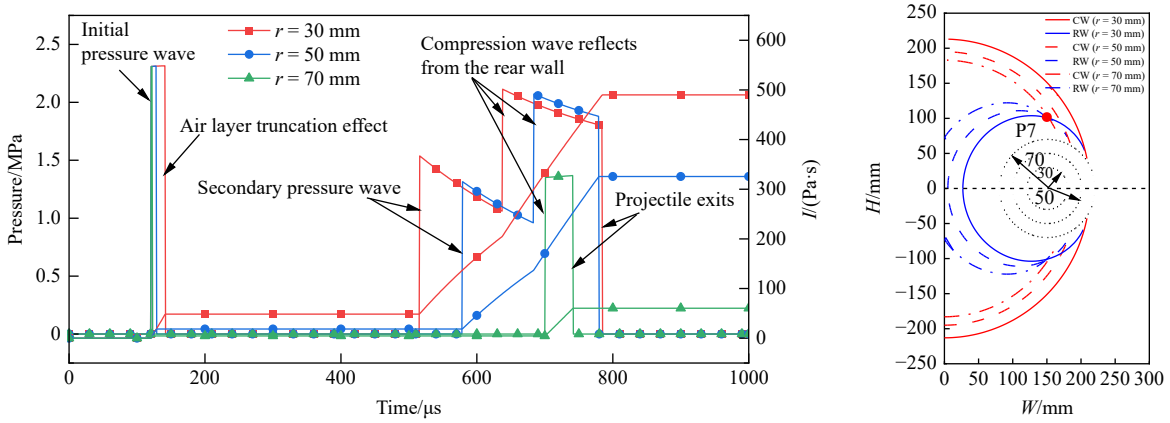


Fig.13 Time history curves of pressure and specific impulse vs. spherical air layer radius r and propagation of rarefaction waves reflected from air layer interfaces

As shown in Fig.13, a larger r leads to a wider influence range of the rarefaction wave from the air layer, and both the initial pressure wave Zone I and the secondary pressure wave Zone II become smaller. As r increases, the attenuation rate of specific impulse for the initial pressure wave reaches as high as 90.5%, and the attenuation rates for the peak and specific impulse of the secondary pressure wave are 14.4% and 33.5%, respectively (comparing $r=30$ mm and $r=50$ mm only). When $r=70$ mm, point P7 enters Zone I (see Fig.6), and is no longer subjected to the secondary water entry pressure wave. However, the compression wave of the secondary pressure wave reflected from the rear wall still causes a delayed pressure peak at P7.

4 Conclusions

This study establishes a computational model for projectile water-entry pressure waves considering reflection from preset air layers. The model is based on both virtual and real mirror methods combined with potential flow theory. Its validity is verified through numerical simulations. Based on the conducted research, the main conclusions are as follows:

(1) The rarefaction wave reflected at the air layer interface induces a truncation effect on the pressure wave within the liquid, significantly reducing the positive pressure duration and the specific impulse of the pressure wave.

(2) An increase in the free surface height h shortens the time for the rarefaction wave to reach the pressure point, causing earlier truncation. When h increases from 30 mm to 90 mm, the attenuation rate of specific impulse at the pressure point rises to 7.6%.

(3) When a spherical air layer is preset along the trajectory, a smaller spherical center distance D leads to earlier truncation of the initial pressure wave by the rarefaction wave, with the specific impulse reduced by up to 87%. A larger D results in attenuation rates of up to 49.3% and 56.4% for the peak pressure and specific impulse of the secondary pressure wave, respectively.

(4) A larger spherical air layer radius r expands the influence range of the rarefaction wave reflected from the air layer and significantly attenuates the specific impulse of the initial pressure wave, as well as the peak value and specific impulse of the secondary pressure wave.

References

[1] Truscott T T, Techet A. Water entry of spinning spheres[J]. Journal of Fluid Mechanics, 2009, 625: 135–165.

[2] Lin J, Luo B, Xu M, et al. Progress of aluminium projectile impacting on plate with hypervelocity[J]. Chinese Journal of High Pressure Physics, 2019, 33: 164–196.

[3] Zou D, Hao Y, Wu H, et al. Safety assessment of large-scale all steel LNG liquid-filled tanks under wind-borne missile impact[J]. Thin-Walled Structures, 2022, 174: 109078.

[4] Jin J, Li D, Hou H, et al. Attenuation effect of a preset bubble on hydrodynamic ram induced by fragments impacting liquid-filled tank[J]. Thin-Walled Structures, 2023, 192: 111085.

[5] Wu M, Jin J, Hou H. Experimental study on the anti-penetration characteristics of liquid-filled structure with air layer[J]. Defence Technology, 2025.

[6] Deletombe E, Fabis J, Dupas J, et al. Experimental analysis of 7.62 mm hydrodynamic ram in containers[J]. Journal of Fluids and Structures, 2013, 37: 1–21.

[7] Artero-Guerrero J A, Pernas-Sánchez J, Varas D, et al. Numerical analysis of CFRP liquid-filled tubes subjected to high-velocity impact[J]. Composite Structures, 2013, 96: 286–297.

[8] Ren K, Wang W, Qing H, et al. BPNN-based prediction for the shapes of a petal hole induced by hydrodynamic ram[J]. Thin-Walled Structures, 2024, 112488.

[9] Fourest T, Deletombe E, Faucher V, et al. Comparison of Keller-Miksis model and finite element bubble dynamicssimulations in a confined medium. Application to the hydrodynamic ram[J]. European Journal of Mechanics - B/Fluids, 2018, 68: 66–75.

[10] Disimile P J, Toy N, Swanson L. A large-scale shadowgraph technique applied to hydrodynamic ram[J]. Journal of Flow Visualization and Image Processing, 2009, 16(4): 303–332.

[11] David T, Nick P, Peter M D. Failure of fluid-filled structures due to high velocity fragment impact[J]. International Journal of Impact Engineering, 2003, 29(1-10): 723–733.

[12] McMillen J H. Shock wave pressures in water produced by impact of small spheres[J]. Physical Review Letters, 1945, 68(9-10): 198–209.

[13] McMillen J H, Harvey E N. A spark shadowgraphic study of body waves in water[J]. Journal of Applied Physics, 1946, 17(7): 541–555.

[14] Disimile P J, Swanson L A, Toy N. The hydrodynamic ram pressure generated by spherical projectiles[J]. International Journal of Impact Engineering, 2009, 36(6): 821–829.

[15] Zhang W, Huang W, Ren P, et al. Characteristics of shock waves generated by horizontal water entry of high-speed projectiles[J]. Journal of Harbin Institute of Technology, 2016, 48(4): 37–41.

[16] Ji Y, Li X, Zhou L, et al. Research progress on hydraulic ram effects induced by high-speed penetrators impacting liquid-filled containers[J]. Journal of Vibration and Shock, 2019, 38(19): 242–252.

[17] Chen T, Guo Z, Zhao G, et al. A discrete method and experimental study for the propagation of shock wave induced by high-speed projectile entering water-filled tanks[J]. Ocean Engineering, 2022, 248: 110835.

[18] Zhao G, Chen T, Jiang X, et al. A visualization system for underwater shock wave shadow imaging of projectile entry and its experimental study[J]. Explosion and Shock Waves, 2022, 42(2): 119–127.

[19] Logvinovich G V. Hydrodynamics of flows with free boundaries[M]. Naukowa: Halsted Press, 1969.

[20] Lee M, Longoria R G, Wilson D E. Ballistic waves in high-speed water entry[J]. Journal of Fluids and Structures, 1997, 11(7): 819–844.

[21] Liu T, Chen C, Cheng Y. A new analytical model for ballistic waves generated by subsonic penetration in water[J]. Ocean

Engineering, 2022, 264: 112472.
[22] Varas D, López-Puente J, Zaera R. Experimental analysis of liquid-filled aluminium tubes subjected to high-velocity impact[J]. International Journal of Impact Engineering, 2009, 36: 81–91.
[23] Townsend D, Park N, Devall P. Failure of liquid filled structures due to high velocity fragment impact[J]. International Journal of Impact Engineering, 2003, 29: 723–733.
[24] Ming F, Zhang A, Yang W. Three-dimensional numerical simulation of the characteristics of underwater explosion shock load near the free surface[J]. Explosion and Shock Waves, 2012, 32(5): 508–514.
[25] Guo Z, Chen T, Zhao G, et al. Hydrodynamic ram analysis in high-speed projectile penetrating into water-filled vessels[J]. Ocean Engineering, 2022, 251: 111092.
[26] Duclaux V, Caille F, Duez C, et al. Dynamics of transient cavities[J]. Journal of Fluid Mechanics, 2007, 591: 1–19.
[27] Aristoff J M, Bush J W M. Water entry of small hydrophobic spheres[J]. Journal of Fluid Mechanics, 2009, 619: 45–78.

考虑预置气层反射的球形弹体入水冲击压力波分析模型

吴蒙蒙[a,b], 侯海量[a], 李　典[a], 杨少红[b], 李永清[a]
（海军工程大学 a. 舰船与海洋学院; b. 基础部, 武汉 430033）

摘要: 为分析球形弹体入水冲击压力波在蓄液结构内的传播过程, 本研究采用虚、实两种镜像方法和势流理论建立了考虑预置气层反射的弹体入水冲击压力波计算模型, 并采用有限元数值计算验证了其正确性。利用所建立的模型分析了在顶部预置层状气层和中心预置球形气层的方形蓄液结构内, 弹体入水压力波传播过程, 并分析了层状气层高度 h、球形气层球心位置 D 和半径 r 对水中压力波强度和传播过程的影响。结果表明, 气层界面反射的稀疏波对蓄液结构内的压力波传播过程产生截断效应, 显著减小了压力波正压作用时间和比冲量, 且比冲量随 h 和 r 的增大而减小。D 越小, 对初始压力波比冲量衰减越显著, 反之, 对二次压力波峰值和比冲量衰减显著。

关键词: 球形弹体; 入水; 压力波; 预置气层; 截断效应
中图分类号: O342　　**文献标识码:** A
基金项目: 国家自然科学基金资助项目(52271338; 51979277; 52371342)

作者简介: 吴蒙蒙(1991−), 女, 博士研究生, 海军工程大学讲师;
侯海量(1977−), 男, 博士, 海军工程大学教授;
李　典(1990−), 男, 博士, 海军工程大学副教授;
杨少红(1975−), 男, 博士, 海军工程大学教授;
李永清(1976−), 男, 博士, 海军工程大学教授。